Supporting Information for Accurate Gap Determination in Monolayer and Bilayer Graphene/*h*-BN Moiré Superlattices

Hakseong Kim,[1] Nicolas Leconte,[2] Bheema L. Chittari,[2] Kenji Watanabe,[3] Takashi Taniguchi,[3] Allan H. MacDonald,[4] Jeil Jung,[5] and Suyong Jung*[1]

[1]*Korea Research Institute of Standards and Science, Daejeon 34113, Korea*

[2]*Department of Physics, University of Seoul, Seoul 02504, Korea*

[3]*Advanced Materials Laboratory, National Institute for Materials Science, 1-1 Namiki, Tsukuba 305-0044, Japan*

[4]*Department of Physics, The University of Texas at Austin, Austin, TX 78712*

[5]*Department of Physics, University of Seoul, Seoul 02504, Korea*

**syjung@kriss.re.kr*

I. DETERMINATION OF TWIST ANGLE IN SINGLE-LAYER GRAPHENE-*H*-BN SUPERLATTICES

A. Twist-angle estimations from multi-probe magneto-conductance measurements

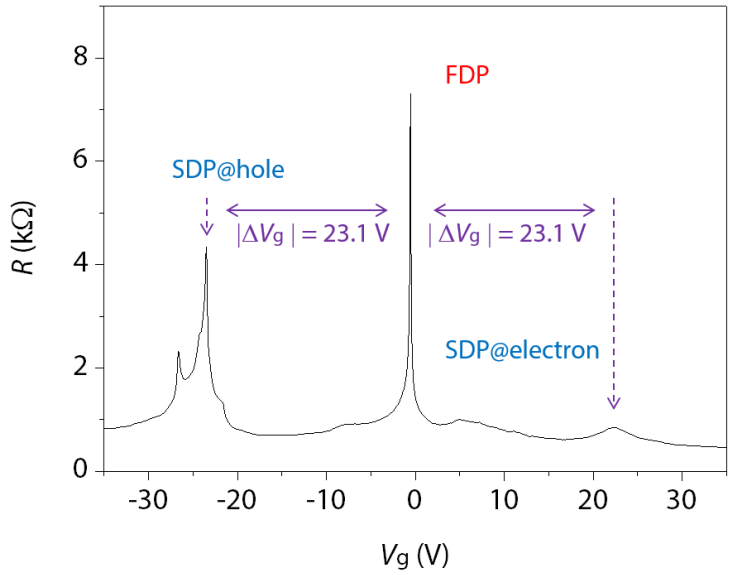

FIG. S1. Resistance vs. external back-gate voltage from the multi-probe graphene-*h*-BN heterostructure with 0.29° as a twist angle.

The twist angles of our graphene-*h*-BN superlattice devices can be determined from the back-gate voltage difference between the first Dirac points (FDP) and second Dirac point (SDP) observed in charge-transfer characteristic curves, as shown in Fig. S1. The position of the SDP (E_{SDP}) with respect to the FDP in energy and moiré wavelength is known to be sensitive to the lattice misalignment and can be estimated from

$$E_{\mathrm{SDP}} = \hbar v_{\mathrm{F}} \sqrt{\pi n} = \frac{2\pi\hbar v_{\mathrm{F}}}{\sqrt{3}\lambda_{\mathrm{M}}} \tag{S1}$$

with

$$\lambda_{\mathrm{M}} = \frac{1.018 a_{\mathrm{cc}}}{\sqrt{2.036\,[1-\cos\theta] + 0.018^2}}, \tag{S2}$$

where $\hbar$, v_{F}, n, λ_{M}, a_{cc} and θ represent the Planck constant, the Fermi velocity, the carrier density, the moiré wavelength, the lattice parameter and the twist angle, respectively. To calculate the charge density for the Fermi level to reach the SDP in single-layer graphene, we first extract the total capacitance C_{tot} of combined back-gate insulators of SiO_2 and bottom h-BN layers by tracing the conductance peaks or resistance dips, each corresponding to individual Landau level in a Wannier-type fan diagram obtained through magnetic-field dependent measurements at $T = 4$ K (Fig. S2). The filling factor ν of single-layer graphene is expressed by following Eq. (S3), so that the carrier density required to fill each Landau level is extracted by locating the evolution of each Landau level as functions of V_{g} and B.

$$\nu = \frac{h}{Be}n = \frac{2\phi_0}{B}n = \frac{2\phi_0}{B}n = \frac{2\phi_0}{B}\frac{V_{\mathrm{g}}C_{\mathrm{tot}}}{e}. \tag{S3}$$

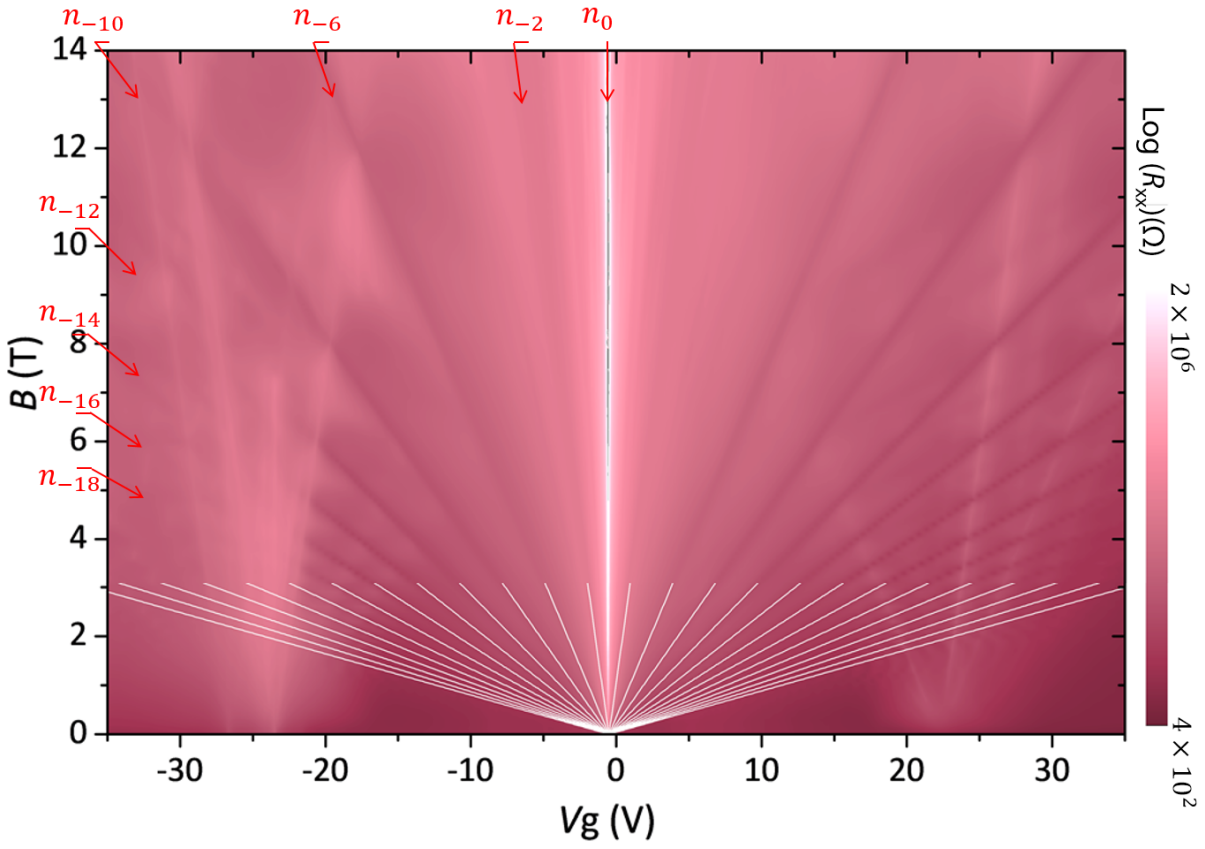

FIG. S2. Wannier-type fan diagram from graphene-h-BN heterostructure

With the estimated n, we can extract the E_{SDP} and λ_{M} using Eq. (S1). Here, we consider

$v_F = 1 \times 10^6$ m/s. Then, the twist angle can be estimated with λ_M from the Eq. (S2). For the twist-angle estimation, we set the lattice parameter a_{cc} equal to 0.246 nm.[S1]

B. Twist-angle estimations from Raman measurements

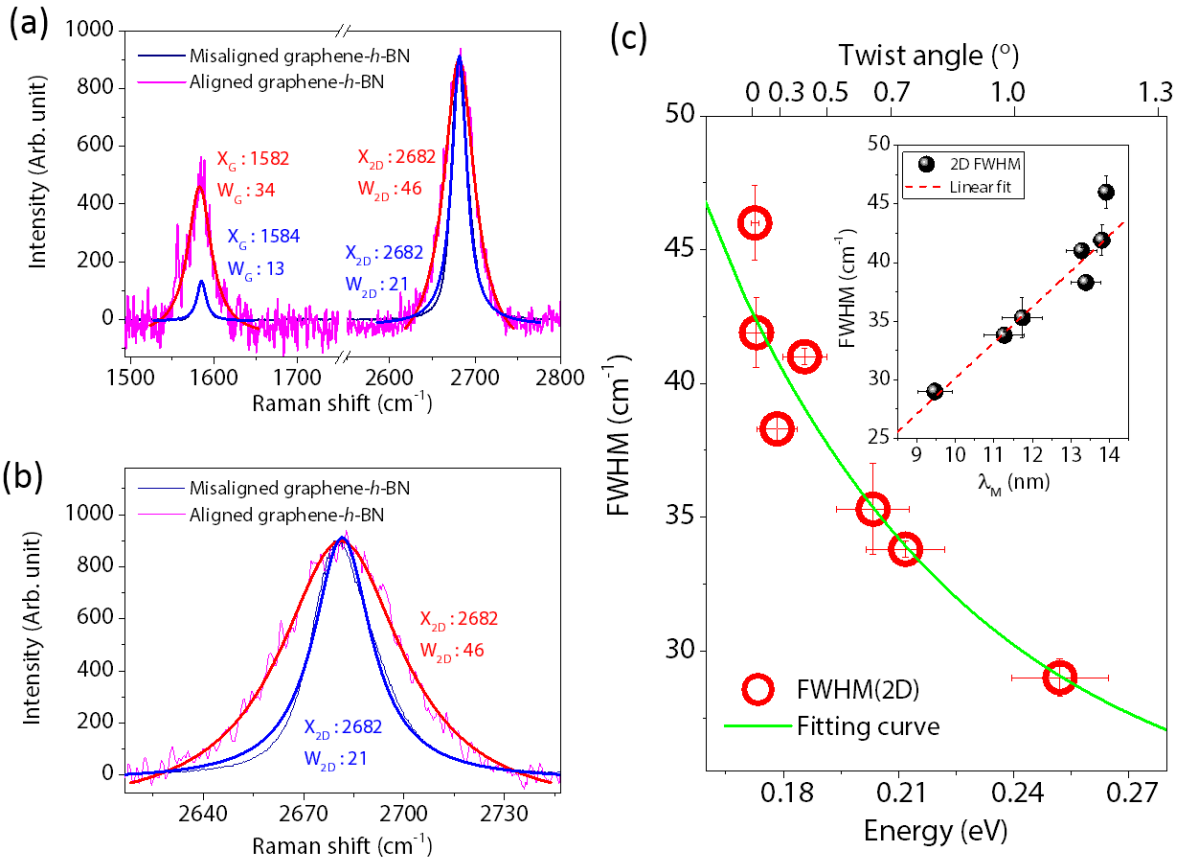

FIG. S3. (a),(b) Comparison of Raman spectra from aligned and misaligned graphene/h-BN devices. (c) Evolutions of FWHM values at varying a twist angle (E_{SDP}). (Inset) FWHM values as a function of the moiré wavelengths.

Raman measurements can be used to determine the twist angle of graphene-h-BN superlattice as well, since the FWHM of 2D peak depends on the moiré wavelength.[S2] Figure S3 shows Raman spectra from aligned and misaligned graphene-h-BN heterostructures, measured with a laser of 532 nm wavelength. As shown in Figs. S3 (a) and (b), the FWHM of the 2D peak from the well aligned graphene/h-BN superlattice is broadened to 46 cm^{-1},

whereas one of the completely misaligned graphene-h-BN heterostructure is around 21 cm^{-1}. At varying twist angles, as shown in Fig. S3(c), the FWHM of 2D peak increases from 29 cm^{-1} to 46 cm^{-1} as E_{SDP} decreases from 0.251 eV ($\theta \approx 1.1°$) to 0.172 eV ($\theta \approx 0°$). Additionally, the 2D FWHM increases linearly as the moiré wavelength increases for the devices with twist angles between 0.13° and 1.1°, with a sudden surge in the FWHM values for tightly aligned graphene-h-BN superlattices with an angle close to 0°. All of these observations are consistent with the report by Eckmann et al..[S2]

II. DETERMINATION OF ENERGY GAPS IN GRAPHENE-H-BN SUPERLATTICES

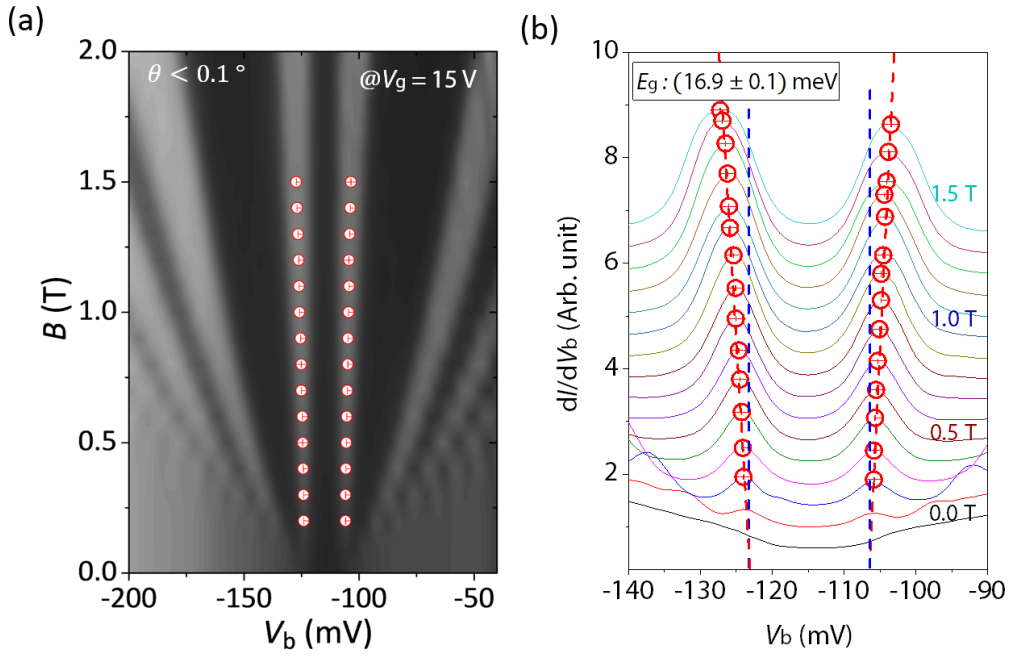

FIG. S4. (a) $\mathrm{d}I/\mathrm{d}V_{\mathrm{b}}$ mapping at $V_{\mathrm{g}} = 15$ V for the device with near 0° twist angle. (b) Evolution of individual $\mathrm{d}I/\mathrm{d}V_{\mathrm{b}}$ spectra at different magnetic fields.

Figure S4 shows a two-dimensional mapping and a series of individual $\mathrm{d}I/\mathrm{d}V_{\mathrm{b}}$ spectra at different B fields from the single-layer graphene-h-BN superlattice in a near perfect alignment ($\theta < 0.1°$). Unlike the misaligned graphene/h-BN, the lowest Landau level (LL_0) in graphene-h-BN superlattice splits to LL_{0-} and LL_{0+} with the energy gap formed in between.

As described in the main text, the size of energy gap can be accurately determined by monitoring the evolution of each Landau level while varying the external magnetic field. The red circles in Figs. S4(a) and (b) indicate $\mathrm{d}I/\mathrm{d}V_\mathrm{b}$ peak positions of LL_{0-} and LL_{0+}. We locate the $\mathrm{d}I/\mathrm{d}V_\mathrm{b}$ peak positions for LL_{0-} and LL_{0+} at different B fields with Lorentzian fittings, and extract the energy gap by linearly extrapolating the LL_{0-} and LL_{0+} peak positions to $B = 0$ T, as displayed in Fig. S4(b).

III. EXTRACTING ENERGY GAPS AT DIFFERENT GATE VOLTAGES

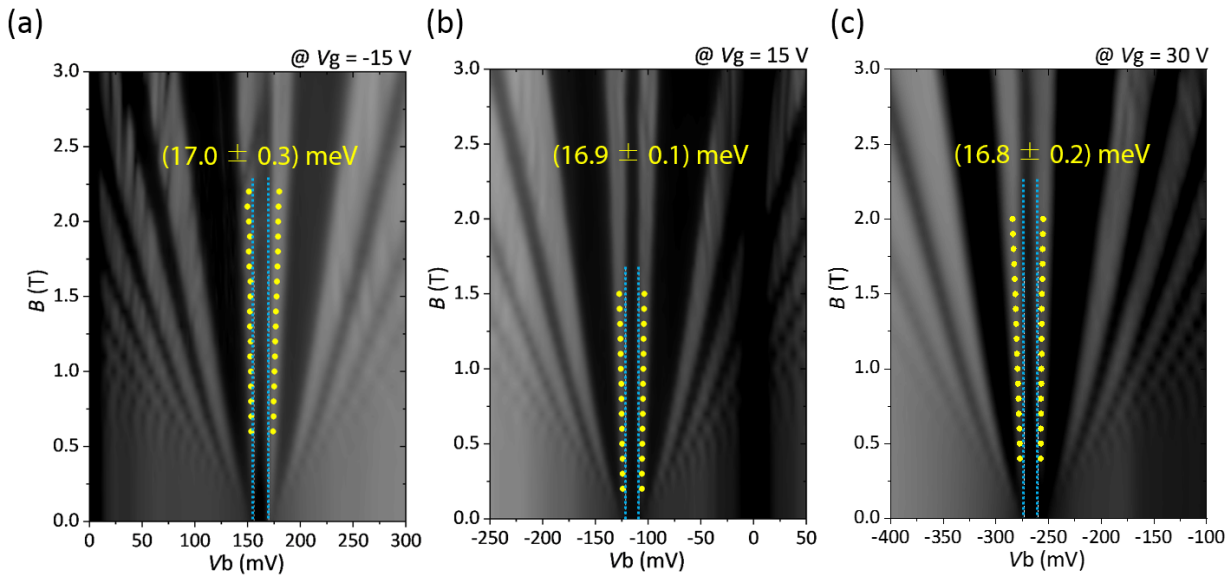

FIG. S5. (a–c) $\mathrm{d}I/\mathrm{d}V_\mathrm{b}$ mappings at different gate voltages of V_g = -15 V, 15 V and 30 V for the device with $\theta < 0.1°$, respectively.

We extract energy gaps at different gate voltages as shown in Figs. S5. Here, yellow dots indicate $\mathrm{d}I/\mathrm{d}V_\mathrm{b}$ peak positions of LL_{0-} and LL_{0+} under different B fields and the V_b spacing between blue dashed lines mark the energy gaps. As expected, extract energy gap does not change its value at different gate voltages.

IV. METHODOLOGY FOR SIMULATION AND THEORY

Electronic band structures are obtained through exact diagonalization of either the continuum model or the corresponding TB model, as outlined in the following sections. DOS calculations at finite magnetic field were done using well established methods of Lanczos recursion[S3,S4] on systems containing about 20 million atoms for both BL and SL. Coupling of the orbital degree of freedom with the magnetic field is incorporated by adding a Peierls phase[S5] to the hopping terms between the carbon atoms.

V. MOIRÉ BANDS MODEL OF SINGLE LAYER GRAPHENE ON *H*-BN

The moiré band Hamiltonian for the SL graphene on h-BN is obtained by considering the moiré band perturbations to the pristine graphene in the form of the following effective Hamiltonian:[S6]

$$H = \hbar v \vec{p} \cdot \vec{\sigma} \tau_0 + H_0(\vec{r}) \sigma_0 \tau_0 + H_z(\vec{r}) \sigma_3 \tau_3 + \vec{H}_{xy}(\vec{r}) \cdot \vec{\sigma} \tau_3 \tag{S4}$$

where the first term captures the physics of pristine graphene and the pseudospin components are given by

$$H_0\left(\vec{r}\right) = 2C_0 \Re e\left[f\left(\vec{r}\right) \exp(i\phi_0)\right], \tag{S5}$$

$$H_z\left(\vec{r}\right) = 2C_z \Re e\left[f\left(\vec{r}\right) \exp(i\phi_z)\right], \tag{S6}$$

and

$$\vec{H}_{xy}(\vec{r}) = 2C_{xy}[\cos(\varphi)(\hat{z} \times \mathbb{1}) - \sin(\varphi)]\vec{\nabla}\, \Re e[e^{i\phi_{xy}} f(\vec{r})], \tag{S7}$$

using the function $f(\vec{r}) = \sum_m \exp(i\vec{G}_m \cdot \vec{r})\ (1 + (-1)^m)/2$ defined from the sum of the six smallest reciprocal lattice vectors $\vec{G}_m$ of the moiré pattern. The off-diagonal element of the moiré pattern Hamiltonian is $H_{AB}(\vec{r}) = (\vec{H}_{xy}(\vec{r}) \cdot \vec{\sigma})_{AB}$. We use the parameters as introduced in Ref. [S7]: $C_0 = 10.13$ meV, $\phi_0 = 146.53°$, $C_{xy} = 11.34$ meV, $\phi_{xy} = \phi_{AB} + \pi/6 = -109.60°$, $C_z = 9.01$ meV and $\phi_z = 68.43°$. G_1 is equal to $4\pi/(3a)$ where the explicit expression for H_{AB} is also provided.

The corresponding TB mapping is readily found as reminded here. The off-diagonal term of the Hamiltonian consists of an unperturbed contribution H^0_{AB} and a moiré pattern term

that we model through δ_1, δ_2 and δ_3

$$H_{\mathrm{AB}}(\vec{k}) = H^0_{\mathrm{AB}} + \delta_1 e^{ik_y a/\sqrt{3}} + \delta_2 e^{-ik_y a/2\sqrt{3}} e^{-ik_x a/2} + \delta_3 e^{-ik_y a/2\sqrt{3}} e^{ik_x a/2},$$

by writing each hopping term as the sum $t_i = -t_0 + \delta_i$. The low-energy expansion near $\vec{K} = (4\pi/3a, 0)$ leads to[S4]

$$H_{\mathrm{AB}} = H^0_{\mathrm{AB}} + \delta_1 - \frac{\delta_2 + \delta_3}{2} + i\frac{\sqrt{3}}{2}(\delta_3 - \delta_2). \tag{S8}$$

After some calculations we find that the moire pattern local hopping amplitudes are given by

$$\delta_1 = \frac{2}{3}\Re e(H_{\mathrm{AB}}), \qquad \delta_{2,3} = \frac{-\Re e(H_{\mathrm{AB}}) \mp \sqrt{3}\,\Im m(H_{\mathrm{AB}})}{3}. \tag{S9}$$

where $\Re e(H_{\mathrm{AB}})$ and $\Im m(H_{\mathrm{AB}})$ are evaluated at the Brillouin-zone corner K.

We note that the SDP band gaps are inherently captured by the model, while the FDP band gap is included by incorporating an additional mass-term with angle-dependent amplitudes predicted by DFT simulations.[S8] One notes that by locally increasing or reducing relaxation, and thus modifying the parameters, one can modify the size of both gaps.[S6]

VI. ON THE SCALING OF THE SECONDARY GAP OF SL WITH TWIST ANGLE

In Ref. [S6], scaling laws for the secondary and primary gaps at the K point were proposed for the SLG/BN system. For the SDP, this law is strictly valid at the K_1-point only and *can* miss the reality that band gaps and overlaps can be indirect, as illustrated in Fig. S6 for a series of angles where light green corresponds to a zero twist angle and dark green is 1.2°. The values in between are 0.4° and 0.8°. One observes that for 0.8°, the secondary gap has become indirect between the K_1 and the maximum around the M point. The gap further overlaps and is completely closed for an angle of 1.2°. We rationalize the smoother transition (and slightly earlier onset) in gap-closing seen experimentally by the observation that the band at the M point, which is responsible for the gap-closing, is flatter and does contain an increased amount of states making this band more sensitive to disorder broadening effects.

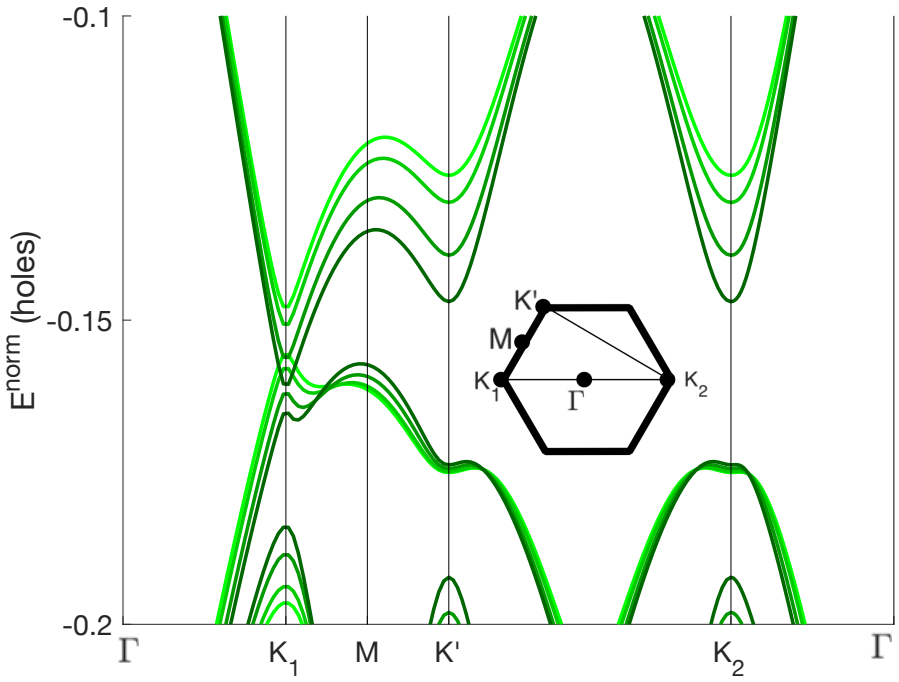

FIG. S6. Band overlap and gap closing with increasing twist angle α for the SDP on the hole side (negative energies). The energies are renormalized with a factor $l_M^\alpha / l_M^{\alpha=0}$ (where l_M^α is the moire length for a chosen value of α) to ease comparison between angles. The values of α range from 0° to 1.2° in increments of 0.4°, going from light green to dark green colors. The gap closing is triggered by the band showing increasing overlapping behavior around the M point. The electronic band structure is represented in the Moire brillouin zone with high symmetry k-points conventions illustrated in the inset.

VII. MOIRÉ BANDS MODEL OF BILAYER GRAPHENE ON HBN

The low energy Hamiltonian for a bilayer graphene is

$$H_{\mathrm{bi}}^{\nu,\xi} = \frac{v_0^2}{(-t_1)} \begin{pmatrix} 0 & \left(\pi^\dagger\right)^2 \\ \pi^2 & 0 \end{pmatrix} + \Delta\sigma_z + H_N^{\mathrm{R}} + H_\xi^{\mathrm{M}}, \tag{S10}$$

where $\pi = (\nu p_x + i p_y)$ where $\nu = \pm 1$ represents the valley index. The remote hopping corrections are given by

$$H_N^{\mathrm{R}} = -\upsilon_3 \begin{pmatrix} 0 & \pi \\ \pi^\dagger & 0 \end{pmatrix} + \frac{\upsilon_3 a}{4\sqrt{3}\hbar} \begin{pmatrix} 0 & \left(\pi^\dagger\right)^2 \\ \pi^2 & 0 \end{pmatrix} + \frac{2\upsilon\upsilon_4}{t_1} \begin{pmatrix} \pi^\dagger\pi & 0 \\ 0 & \pi\pi^\dagger \end{pmatrix} + \frac{\Delta'\upsilon^2}{t_1^2} \begin{pmatrix} \pi^\dagger\pi & 0 \\ 0 & \pi\pi^\dagger \end{pmatrix},$$

where the effective hopping parameters are $t_0 = -2.61$ eV, $t_1 = 0.361$ eV, $t_3 = 0.283$ eV and $t_4 = -0.138$ eV[S9], where the associated velocities are defined as $\upsilon_m = \sqrt{3}a\,|t_m|/2\hbar$ with $a = 2.46\,\mathring{A}$ the lattice constant of graphene. The diagonal term $\Delta' = 0.015$ eV is used to provide an accurate fit for the LDA bands.

The moiré pattern term is given by

$$H^M_{\xi=\pm1}(\vec{r}) = V^M_{A/B}(\vec{r}) = 2C_{A/B}\mathrm{Re}\left[e^{i\phi_{A/B}} f(\vec{r})\right] \frac{(\xi\sigma_z + \mathbb{1})}{2} \tag{S11}$$

where we have used the parameters $C_A = -14.88$ meV, $\phi_A = 50.19^\circ$ [S7,S8] have been used together with the auxiliary function $f(\vec{r}) = \sum_{m=1}^{6} e^{i\vec{G}_m\cdot\vec{r}}(1+(-1)^m)/2$ that we have expressed using the six moiré reciprocal lattice $\vec{G}_{m=1\ldots6} = \hat{R}_{2\pi(m-1)/3}\vec{G}_1$ that is successively rotated by sixty degrees where $\vec{G}_1 = (0, 4\pi/(\sqrt{3}\ell_M))$, where the moiré pattern length is given by $\ell_M \simeq a/(\varepsilon^2+\theta)^{1/2}$ that depends on $\varepsilon = (a-a_{BN})/a_{BN}$ the relative lattice constant mismatch between graphene and BN, and the twist angle θ. The parameter $\xi = \pm 1$ distinguishes the two types of possible alignments between TLG and BN and for our calculations we have chosen to represent only the $\xi = 1$ case corresponding to potential $V^M_A(\vec{r})$.

For the TB model of BL graphene, we use the single structure factor model as proposed in Ref. [S9]. This approximation folds all the physical hopping parameters of BLG down to an effective model with only nearest neighbor and on-site or purely vertical type hoppings. The TB parameter conventions are illustrated in Fig. S1. Hopping terms $t_{BA'}$, t_{AB}, $t_{AA'}$ $(= t_{BB'})$ and $t_{AB'}$ are set to 0.33 eV, -3.0 eV, 0.09 eV and 0.14 eV respectively. While restricting the number of parameters, this model still tends to the same continuum limit as the full tight-binding model. It captures all relevant features, especially the required trigonal warping and electron-hole asymmetry, acting as prerequisites to observe the band overlap at higher energy once the h-BN induced moire interaction is included.[S10] Onsite energies for

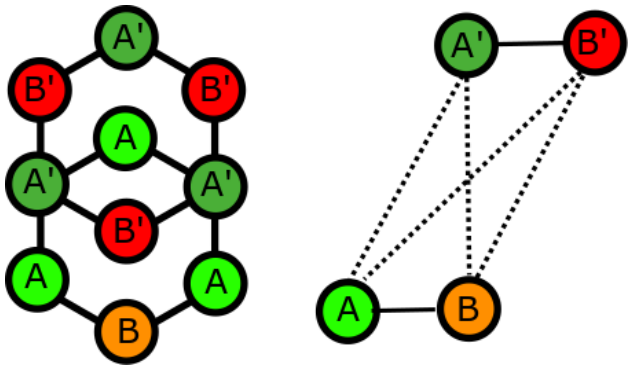

FIG. S7. Single structure factor model as proposed in Ref. [S9]. Hopping terms $t_{BA'}$, t_{AB}, $t_{AA'}$ (= $t_{BB'}$) and $t_{AB'}$ are set to 0.33 eV, −3.0 eV, 0.09 eV and 0.14 eV respectively. Onsite energies are set to zero before inclusion of the moire effective Hamiltonian perturbations.

the bare BL model are considered equal to zero before introducing the h-BN interactions to the bottom layer of graphene. The same procedure as outlined for the TB model of SL is used to incorporate the moiré effects into the bottom layer of graphene only.

VIII. MOIRE POTENTIAL INDUCED BROADENING OF EDGE STATES

To provide further insight as to the origin of the additional tunneling channels that are picked up in all our samples that are deposited on h-BN, as compared to the control samples free from any h-BN moiré potential effects where no such channels are observed, and that manifest themselves as a shaded feature inside the electric-field induced gap (see Fig. 6 of main text), we provide in Fig. S8 the results of our simulations on zigzag ribbons of BL deposited on h-BN where the width is set to 4 times the moiré period. This system contains about 40000 atoms and is simulated using PyBinding[S12]. The upper left panel calculates the 1-D electronic band-structure for the TB model of the BL ribbon in absence of electric field, while the top right panel includes an electric field of 0.1 eV thus causing a band gap opening where one can observe the topological edge states crossing the Fermi energy[S11]. In the lower panels, the effect of the moiré potential is included and shows a broadening of the energy range of the states at the band edges. In presence of an electric field, in the lower right panel, we observe an electron-hole asymmetric broadening of these states, thus obfuscating part of the band-gap and seemingly also part of the topological states. We claim that this

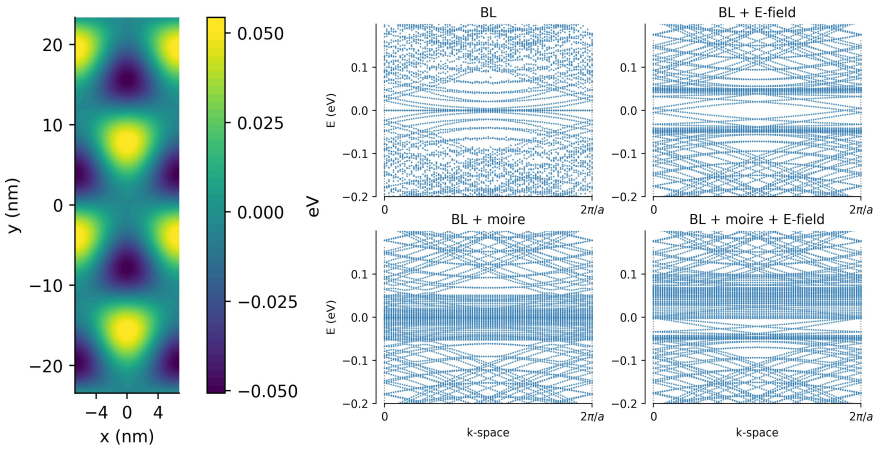

FIG. S8. TB simulations of bilayer zigzag graphene nanoribbons. The surface plot on the left shows the modulation of the onsite energies due to a moiré potential [only the term from Eq. (S5), without sublattice dependent mass-term, for aesthetic reasons] where the width of the ribbon in the y-direction corresponds to 4 times the moiré period and the x-direction is repeated periodically and the panels on the right provides the electronic band-structures in presence and absence of electric field and/or h-BN induced moiré potential. Only in presence of a moiré potential we observe a broadening of the states at the band-edges around the electric field induced band-gap thus explaining the shaded feature observed inside the gap in our experiments.

asymmetric broadening can explain the observed shade inside the gap. In this simulation, we include the mass-term of Eq. (S6) only, without qualitative loss due to the absence of the other terms from Eq. (S4). One should probably aim to minimize this broadening effect if one's goal is to study the topological edge states.

IX. BERRY CURVATURE OF LOW-ENERGY BANDS OF BL/*H*-BN SYSTEM

For further reference, in Fig. S9, we calculate the band structure and Berry curvatures of the low energy bands that can be topological in nature.

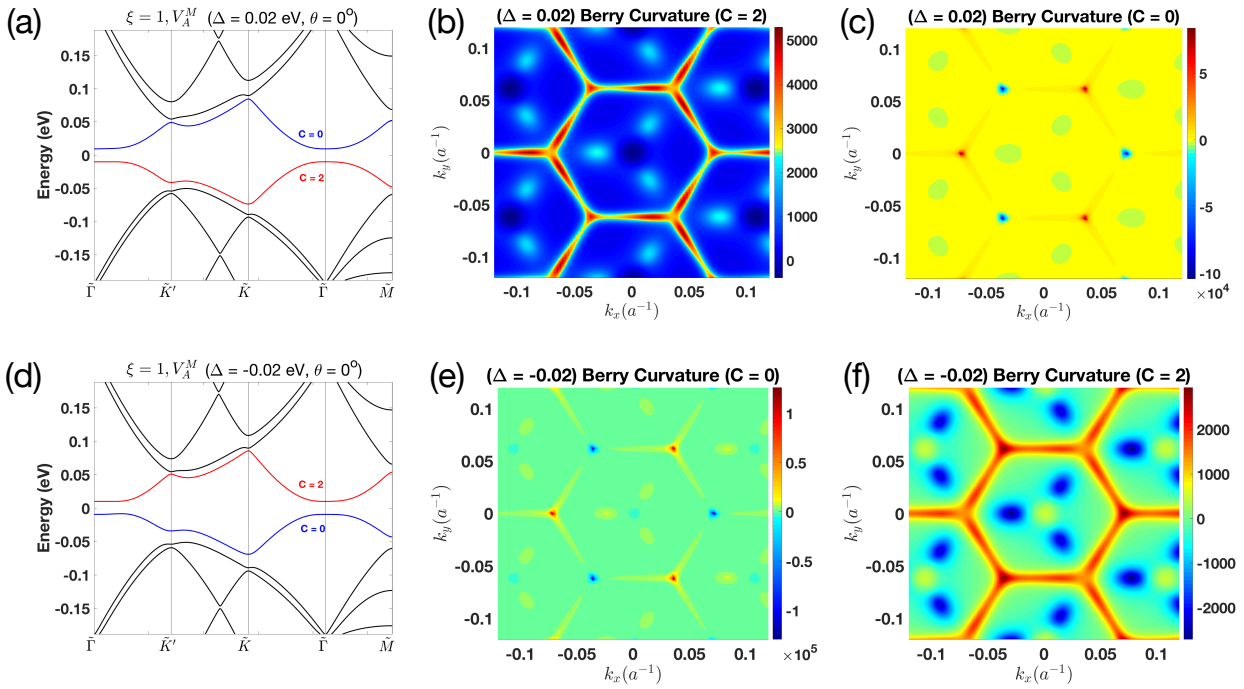

FIG. S9. (a) Moiré bands of bilayer graphene under a positive $\Delta = 0.02$ eV and moiré potential V_A^M giving rise to a finite Chern number for the valence bands, and (b, c) associated Berry curvatures for the low energy valence and conduction bands. (d) Moiré bands under a reversed interlayer potential difference $\Delta = -0.02$ eV. We notice that the Chern bands switch from valence to conduction band, and the (e–f) associated Berry curvatures for valence and conduction bands.

[S1] Liu, M., Springer. **56** (2017)

[S2] Eckmann A., Park J.S., Yang H.F., Elias D., Mayorov A.S., Yu G.L., Jalil R., Novoselov K.S., Gorbachev R.V., Lazzeri M., Geim A.K., and Casiraghi C., Nano Lett. **13**, 5242-5246 (2013).

[S3] N. Leconte, A. Lherbier, F. Varchon, P. Ordejon, S. Roche, and J.-C. Charlier, Phys. Rev. B **84**, 235420 (2011).

[S4] N. Leconte, A. Ferreira, and J. Jung, in *Semiconductors and Semimetals* (Elsevier, 2016) pp. 35–99.

[S5] J. M. Luttinger, Phys. Rev. **84**, 814 (1951).

[S6] J. Jung, E. Laksono, A. M. DaSilva, A. H. MacDonald, M. Mucha-Kruczyński, and S. Adam, Phys. Rev. B **96**, 085442 (2017).

[S7] J. Jung, A. Raoux, Z. Qiao, and A. H. MacDonald, Phys. Rev. B **89**, 205414 (2014).

[S8] J. Jung, A. M. DaSilva, A. H. MacDonald, and S. Adam, Nature Communications **6**, 6308 (2015).

[S9] J. Jung and A. H. MacDonald, Phys. Rev. B **89**, 035405 (2014).

[S10] M. Mucha-Kruczyński, J. R. Wallbank, and V. I. Fal'ko, Phys. Rev. B **88**, 205418 (2013).

[S11] Jung, Jeil and Zhang, Fan and Qiao, Zhenhua and MacDonald, Allan H., Phys. Rev. B **7**, 075418 (2011)

[S12] Moldovan, Dean and Andelkovic, Misa and Peeters, Francois, pybinding v0.9.4: a Python package for tight-binding calculations